Int J Adv Manuf Technol (2016) 84:895–906
DOI 10.1007/s00170-015-7754-2

ORIGINAL ARTICLE

Comparative study of ductile fracture prediction of 22MnB5 steel in hot stamping process

Dongyong Shi[1] · **Ping Hu**[2] · **Liang Ying**[2]

Received: 13 April 2015 / Accepted: 26 August 2015 / Published online: 5 September 2015

Abstract Damage growth and ductile fracture prediction is an urgent question for hot stamping operations. Numerous models for ductile fracture prediction in cold forming processes have been extensively developed. There is a real need to compare them to choose the best suitable one for hot stamping applications. In the present study, several ductile fracture criteria under the category of "uncoupled phenomenological criterion" and the "fully coupled damage criterion," i.e., the continuum damage mechanics (CDM)-based Lemaitre model, were employed to compare their prediction capability on ductile failure prediction. These two categories of criteria were coded into an explicit thermo-mechanical finite element code dedicated to hot stamping simulation. Both hot forming limit and hot tensile tests of 22MnB5 steel were conducted in order to provide suitable data for calibrating these models. Numerical results of the applications of these models to the hot stamping process simulation of an automotive B-pillar were compared with the experimental ones. It is concluded that thermo-mechanical finite element analysis in conjunction with CDM-based Lemaitre model can be used as a reliable tool to predict ductile damage and fracture of 22MnB5 steel in hot stamping process.

Keywords Hot stamping · 22MnB5 · Ductile fracture · Damage · Finite element simulation

✉ Liang Ying
yingliang@dlut.edu.cn

[1] Department of Engineering Mechanics, Dalian University of Technology, Dalian 116024, People's Republic of China

[2] School of Automotive Engineering, Dalian University of Technology, Dalian 116024, People's Republic of China

1 Introduction

In modern automobile industry, to reduce the weight of automobiles and decrease gas emissions while maintaining crash performance, more and more advanced high- and ultra-high-strength steels have been used to produce automotive structural parts. However, cold stamping of the mentioned steels is met with many difficulties, such as large forming force, considerable springback, and low formability. As an alternative to the conventional press forming, hot stamping is recognized as the best solution to these problems, allowing lower loads on tools, higher precision, and better formability of formed parts [1, 2]. The process mainly consists of austenization of the boron steel blank in a furnace, transferring to the press, forming at elevated temperatures, and quenching between the press tools with cooling system. In contrast to conventional cold stamping, the elevated temperature not only decreases the flow stress but also improves the ductility and formability of the steel sheets. However, the formability may deteriorate due to the unsuitable design of die-face or processing parameters, such as forming temperature, blank holding force, and friction condition between the blank sheet and the tools.

The formability of sheet metal at room temperature is often evaluated by a forming limit curve (FLC). It is a strain-based diagram typically drawn with the horizontal and vertical axes as minor and major strains at failure, respectively. FLC for metal sheets is commonly determined from test pieces stretched to failure by either a test with a flat punch as described by Marciniak and Kuczyński [3] or a test with a hemispherical punch as developed by Nakazima et al. [4]. In accordance with the test method for FLC at room temperature, there are several reports as regards investigation on forming limits of boron steel at elevated temperature [5–9]. However, hot stamping is a non-isothermal process. Therefore, the FLC determined for specific forming conditions, usually a defined

temperature and strain rate, is not sufficient for predicting the fracture in the whole process. So far, there is a lack of a valuation method for evaluating the formability of work piece during hot stamping process.

The fracture surface of the boron steel sheet tested at elevated temperatures exhibits ductile fracture characteristics, which have been indicated by Güler et al. [10]. Ductile fracture often results from the nucleation, growth, and coalescence of micro-voids in metals and alloys under severe plastic deformation. Regarding the modeling and prediction of ductile fracture, two main approaches have been extensively used and developed: uncoupled phenomenological models (or ductile fracture criteria) and coupled phenomenological models (or damage mechanics). For the uncoupled phenomenological ductile fracture criteria, the interaction between the strain or stress behavior and the damage is neglected and only a post-processing of an indicator variable is adopted after a classical structure analysis. An integrated product of the equivalent plastic strain increment was employed as the indicator variable to predict material failure when its critical value is reached. However, the fully coupled damage criteria incorporate damage accumulation in the constitutive equations. They represent the physical background of micro-mechanical fracture. A number of criteria for ductile fracture [11–16] were proposed to describe fracture behavior of metals based on various assumptions. These criteria have been applied to predict the ductile failure in sheet metal forming processes. Ozturk and Lee [17] utilized various fracture criteria for the prediction of the forming limit of AKDQ steel sheet. Takuda et al. predicted the fracture initiation for deep drawing processes of the laminated composite sheets [18] and limiting strains for aluminum alloy sheets in biaxial stretching [19] using ductile fracture criterion. Liu et al. [20] introduced a ductile fracture criterion to finite element simulations for the fracture prediction in bore expanding, hemispherical punch bulging, and deep drawing of sheet metals. Lou et al. [21] proposed a micro-mechanism-motivated ductile fracture model to predict the fracture forming limit diagram of DP780 from the uniaxial tension to the balanced biaxial tension. Ogawa et al. [22] utilized Oh ductile fracture criterion [12] to predict the formability of Mg alloy at elevated temperatures for precision forging.

Damage-mechanics-based models [23–25] have also been developed to predict the damage growth and the ductile fracture in various metal forming processes. Abbassi et al. [26] employed the Gurson–Tvergaard–Needleman (GTN) damage mechanics model [24] to evaluate the ductile damage and fracture phenomena during elliptical bulge and Erichsen tests of stainless steel 304. A predictive damage model, based on the theory of damage-plasticity, was proposed by Khelifa et al. [27] to predict the onset of macroscopic cracks in thin sheet metals during deep drawing operation at room temperature. Aboutalebi et al. [28] implemented a fully coupled elastic–plastic damage model into an explicit code to predict damage propagation and crack initiation, and ductile fracture behavior of St14 steel. Mkaddem et al. [29] simulated the damage evolution and rupture in wiping die bending processes by employing GTN and continuum damage mechanics (CDM) damage models. Bariani et al. [30] predicted the isothermal FLC of 22MnB5 based on CDM and finite element software Forge2008. The FLC determined in the numerical prediction is in good agreement with the experimental one. Mohamed et al. [31] established a set of coupled viscoplastic damage constitutive equations for predicting formability of AA6082 aluminum alloys in warm forming conditions. And, the damage model was calibrated using uniaxial tensile data at elevated temperatures.

In this study, the ductile fracture of 22MnB5 steel during hot stamping process was predicted by the ductile fracture criteria including the Oh, Brozzo, Ayada, and Rice-Tracey models and CDM-based Lemaitre model, respectively. Hot forming limit tests were carried out to construct the FLCs at different temperatures experimentally. The FLCs constructed with a circle grid analysis (CGA) method were employed to calibrate the critical values for different ductile fracture criteria. And, hot tensile tests were performed to characterize strain hardening properties of 22MnB5 steel and identify the damage parameters involved in the damage model. The calibrated criteria for ductile fracture and CDM-based Lemaitre model were respectively implemented into an explicit thermo-mechanical finite element code. A comparative study between the results obtained by the simulations using the two categories of models is presented and discussed based on the hot stamping experiments of an automotive B-pillar part.

2 Numerical models for ductile fracture

2.1 Criteria for ductile fracture

In sheet metal forming operation, the metallic material experiences severe plastic deformation, which leads to the formation of high strain localization zones. In the microscopic viewpoint, the large irreversible deformation induces the nucleation, growth, and coalescence of micro-voids, and then fracture. In order to predict the occurrence of ductile fracture, numerous authors have proposed their own criteria. Various criteria postulate that fracture occurs when the integrated product of the

equivalent plastic strain increment and a function depending on stress components reaches a critical value:

$$\int_0^{\bar{\varepsilon}_f} F(\sigma_{ij})\, d\bar{\varepsilon}^p = C \tag{1}$$

where F is the weighting function, which is generally a function of the components or invariants of the stress tensor σ_{ij}, $\bar{\varepsilon}^p$ is the equivalent plastic strain, $\bar{\varepsilon}_f$ is the equivalent plastic strain to fracture, and C is the critical value of the material.

In this study, the following empirical types of ductile fracture criteria were utilized.

According to Cockcroft–Latham criterion [11], the fracture is controlled by the maximum principal tensile stress integrated over the equivalent plastic strain path. Oh et al. [12] modified the Cockcroft–Latham criterion [11] by normalizing the maximum principal tensile stress by the equivalent stress. Their criterion states that the fracture in a ductile material occurs when

$$\int_0^{\bar{\varepsilon}_f} \frac{\sigma_1}{\bar{\sigma}} d\bar{\varepsilon}^p = C_1 \tag{2}$$

where σ_1 is the maximum principal tensile stress and $\bar{\sigma}$ is the equivalent stress.

Brozzo et al. [13] adjusted the Cockcroft–Latham criterion [11] by considering the effect of hydrostatic pressure based on their experimental results. And, the modified criterion can be expressed by a function of the maximum principal stress and the hydrostatic pressure:

$$\int_0^{\bar{\varepsilon}_f} \frac{2\sigma_1}{3(\sigma_1 - \sigma_m)} d\bar{\varepsilon}^p = C_2 \tag{3}$$

where σ_m is the hydrostatic pressure expressed as $(\sigma_1+\sigma_2+\sigma_3)/3$, and σ_2 and σ_3 represent the medium and minimum principal stresses, respectively.

Ayada et al. [14] proposed a criterion allowing for the history of stress triaxiality affecting the occurrence of the ductile fracture. The criterion is written as

$$\int_0^{\bar{\varepsilon}_f} \eta\, d\bar{\varepsilon}^p = C_3 \tag{4}$$

where η is the stress triaxiality expressed as $\eta = \sigma_m/\bar{\sigma}$.

In order to describe how the stress state affects the evolution of spherical voids, Rice and Tracey [15] proposed a criterion by introducing the exponent function of the stress triaxiality:

$$\int_0^{\bar{\varepsilon}_f} \exp(1.5\eta)\, d\bar{\varepsilon}^p = C_4 \tag{5}$$

As described above, these four different ductile fracture criteria adopt different weighting functions. Based on the von Mises isotropic yield function, the different weighting functions depending on the strain path are presented in Fig. 1.

The determination of these critical values C_1 to C_4 is the key to the numerical prediction of the ductile fracture. To identify these critical values, destructive tests have to be carried out under at least one or two types of strain conditions [32]. In addition, in order to apply these ductile fracture criteria to the hot stamping domain, the critical values C_1 to C_4 may be thought as temperature and strain rate dependent.

2.2 CDM model

In CDM, the scalar D ($0 \le D \le 1$) is introduced as an internal variable to indicate the degree of the isotropic damage in the material when subjected to loading conditions. It is defined as the ratio of damaged area A_D to the total surface A: $D = A_D/A$. And, a macroscopic crack is initiated when the damage factor D reaches a critical value D_{cr} which is a material constant. According to the principle of strain equivalence, the effective stress is defined as the one that should be applied to an undamaged material. It is given by

$$\tilde{\sigma}_{ij} = \frac{\sigma_{ij}}{1-D} \tag{6}$$

Instead of the Cauchy stress, the effective stress is used in the constitutive equations to describe the impact of damage on the macroscopic mechanical behavior of materials.

The energy density release rate Y, the variable associated with D, is derived from the state potential as follows [33]:

$$Y = \frac{\bar{\sigma}^2}{2E(1-D)^2}\left[\frac{2}{3}(1+\nu) + 3(1-2\nu)\eta^2\right] \tag{7}$$

where E is the temperature-dependent Young's modulus of undamaged elasticity, and ν is the Poisson's ratio which is also

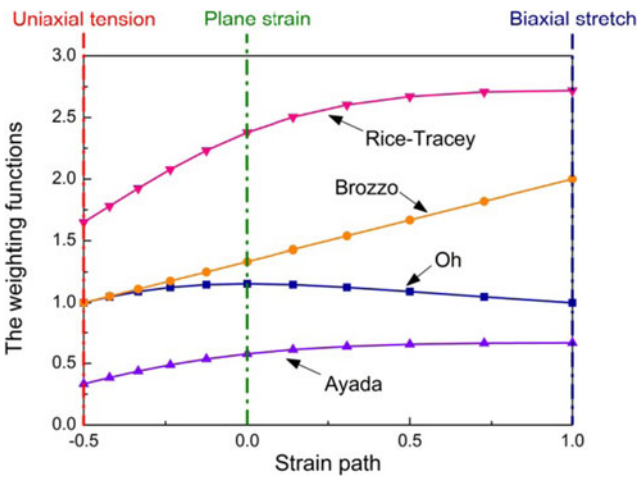

Fig. 1 The different weighting functions for the four ductile fracture criteria depending on the strain path

a function of temperature and not affected by the damage process. According to the thermodynamics of irreversible processes, the dissipation potential should be defined in order to derive the laws of evolution of the state variables associated with the dissipative mechanisms. And, the damage potential F_D is defined as

$$F_D = \frac{S}{(s+1)(1-D)}\left(\frac{Y}{S}\right)^{s+1} \tag{8}$$

where S and s are two damage parameters which depend on temperature and strain rate. Finally, the evolution law of damage is given by

$$\dot{D} = \dot{\lambda}\frac{\partial F_D}{\partial Y} = \frac{\dot{\lambda}}{1-D}\left(\frac{Y}{S}\right)^{s} \tag{9}$$

where $\dot{\lambda}$ is the plastic multiplier. The nucleation of voids at low plastic strain is less noticeable or its presence does not influence material strength. Lemaitre [25] suggested that damage is only activated from a certain level of plastic strain due to the presence of plastic strain threshold for damage initiation. p_D is the damage threshold links with nucleation process and also depends on temperature and strain rate. When the equivalent plastic strain reaches the certain threshold, the presence of voids and its influence are noticeable. And then, damage is activated.

In order to predict the ductile fracture under hot stamping condition, the determination of these three damage parameters (p_D, s, and S) depends on temperature and strain rate is necessary.

3 Experiments and parameter determination

3.1 Material

The material used in this study is a hot rolled 22MnB5 steel sheet with a thickness of 2.0 mm. Table 1 lists the chemical composition and mechanical properties of the tested material in the as-received condition.

3.2 Hot forming limit test

The objective of the hot forming limit test is to identify the critical values C_1 to C_4 in Eqs. (2)–(5). These critical values can be determined by comparing the FLCs predicted by the ductile fracture criteria with the experimental ones. Li et al. [8] investigated the effect of strain rate on the hot forming limit of 22MnB5 steel with numerical method, and they found that the difference among FLCs at different strain rates is small. In addition, the experimental determination of FLCs is time-consuming. Therefore, in this study, the effect of strain rate on the FLC was ignored and an average strain rate of 0.1 s^{-1} was employed. And, the critical values are merely considered temperature dependent.

During hot stamping process, the blanks are generally formed in the range between 650 and 800 °C. Therefore, the hot forming limit tests at 600, 700, and 800 °C were carried out to construct the isothermal FLCs of 22MnB5 steel. The rectangular specimens which have the same length of 180 mm but different widths, varying from 20 mm up to 180 mm, were applied to obtain various strain conditions. The grids with diameter of 2.5 mm were marked on the surface of specimens by a laser marker. The test device is illustrated in Fig. 2. It is mainly made up of the heated Nakazima tool sets, the hydraulic press, the furnace, and the transfer arm. The Nakazima tool sets were composed of a hemispherical punch with the diameter of 100 mm, a blank holder, and a die with the diameter of 110 mm. A draw bead was utilized to prevent material flows. The whole Nakazima tool sets can be heated up to a maximum temperature of 900 °C to keep the temperature of the blank sheet constant during the tests.

During the tests, the tool sets were firstly heated up to the test temperature. The specimens were heated to 900 °C at a rate of 10 °C/s in the furnace and held for 5 min for full austenitization. After austenitization, the specimens were transferred into the tool sets by the transfer arm and rapidly cooled to the test temperature with an average cooling rate of 50 °C/s during the transfer process. Then, isothermal deformation was performed on the specimens until failure happens.

The specimens of 22MnB5 tested are shown in Fig. 3a. The limit strains are approximated using the CGA method by comparing the dimensions of grids marked on specimens before and after deformation as presented in Fig. 3b.

3.3 Hot tensile test

Hot tensile tests were performed on a thermo-mechanical tensile testing machine WDW 100-KN to investigate the damage parameters with respect to temperature and strain rate. Dog-

Table 1 Chemical composition and mechanical properties of the tested material

	Chemical composition (mass%)						Mechanical properties		
Material	C	Si	Mn	P	B	Cr	YS (MPa)	TS (MPa)	EI (%)
22MnB5	0.23	0.18	1.26	0.013	0.0035	0.21	442	574	25.2

YS yield strength, *TS* tensile strength, *EI* elongation

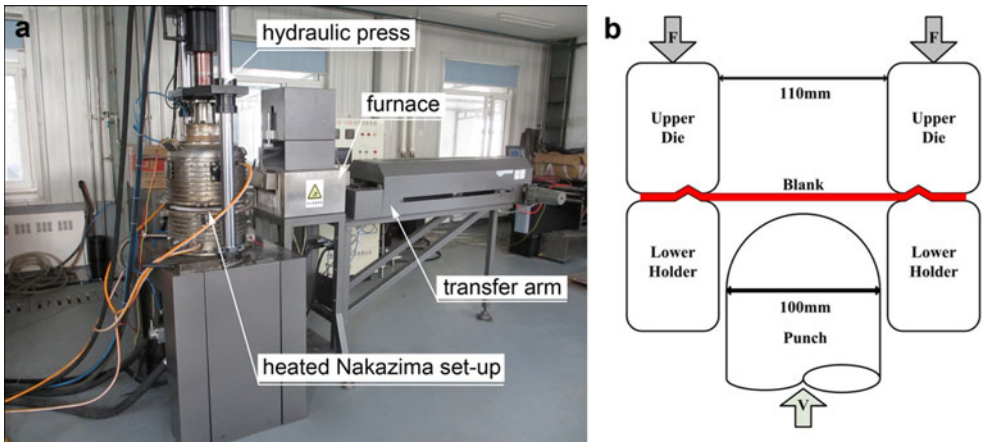

Fig. 2 Hot forming limit tests: **a** the test equipment and **b** the schematic diagram of Nakazima setup

bone specimens with gauge length of 50 mm and width of 20 mm were used in the tests. The tension temperature was varied between 650 and 800 °C, and three different strain rates, 0.01, 0.1, and 1.0 s^{-1}, were applied in order to cover the temperature and strain rate ranges in the actual industrial processes. During the tests, the specimens were first austenitized at 900 °C for 5 min and then cooled to the tension temperature at the cooling rate of 50 °C/s by the compressed-air nozzle. Then, the specimens were isothermally strained up to rupture. And, the axial tensile force and displacement were recorded by the force and displacement sensors, respectively. The experimental equipment and fractured specimens are shown in Fig. 4.

The true stress–true strain curves of 22MnB5 steel at elevated temperatures can be described by the modified Norton–Hoff equation [34]:

$$\sigma = K_0 \cdot \exp\left(\frac{\beta}{T}\right) \cdot (\varepsilon_0 + \varepsilon)^{n(T)} \cdot \dot{\varepsilon}^{m(T)} \tag{10}$$

with $n(T)=n_0 \cdot \exp(-c_n(T-T_0))$ and $m(T)=m_0 \cdot \exp(c_m(T-T_0))$ (11)

The material constants in this equation can be determined from the hot tensile tests by the regression method, and they

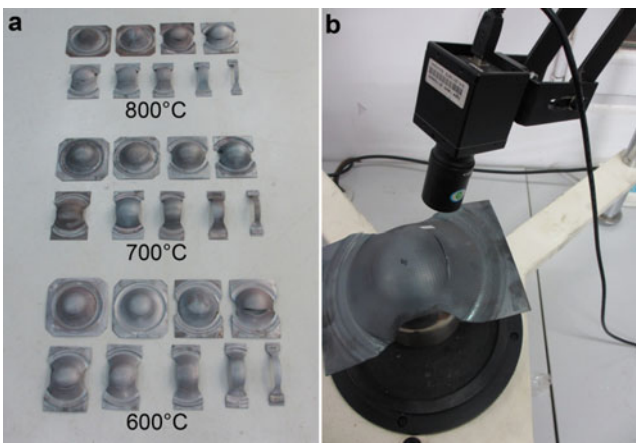

Fig. 3 **a** The finished specimens of 22MnB5steel; **b** limit strains measurement

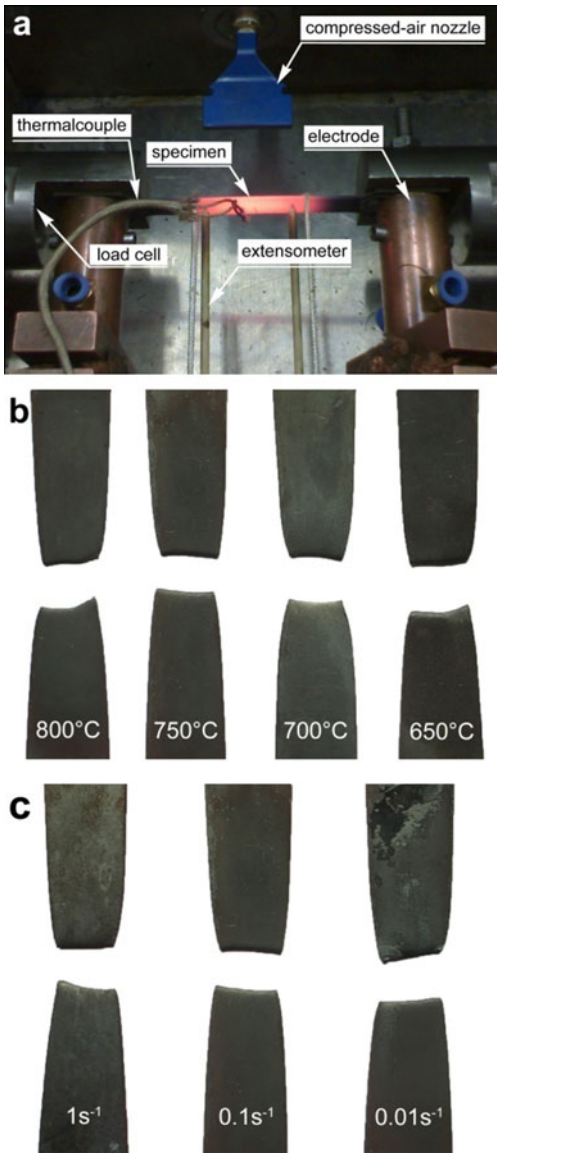

Fig. 4 Hot tensile tests: **a** the test equipment; **b** specimens deformed at a strain rate of 0.1 s^{-1}; and **c** specimens deformed at a temperature of 750 °C

are as follows: K_0= 39.11 MPa, β= 2176.35, ε_0= 0.0012, n_0= 0.2105, c_n= 0.0023, m_0= 0.0602, c_m= 0.0031, and T_0= 500°C. Here, T_0 denotes a reference temperature.

3.4 Parameter determination

3.4.1 Determination of critical values

The prediction of isothermal FLC is based on the von Mises isotropic yield function, which can be described as

$$f = \sigma_1^2 + \sigma_2^2 - \sigma_1\sigma_2 - \sigma_y^2 = 0 \tag{12}$$

where σ_y represents the yield strength.

Based on the Drucker's assumption, the plastic strain increment $d\varepsilon_{ij}^p$ can be expressed as follows:

$$d\varepsilon_{ij}^p = d\lambda \frac{\partial f}{\partial \sigma_{ij}} \tag{13}$$

where $d\lambda$ is the plastic multiplier.

The limit strains for the four ductile fracture criteria can be deduced from the yield function and the plastic strain increment. The critical values of these four ductile fracture criteria were determined by fitting the numerical FLCs to the experimental ones. Table 2 lists the determined temperature-dependent critical values for 22MnB5 steel. FLCs predicted by the four ductile fracture criteria are compared with experimental results as represented in Fig. 5. The experimental results indicate that the formability of 22MnB5 improves significantly as the temperature increases from 600 to 800 °C. For FLCs on the left hand side, the Ayada criterion and the Rice–Tracey criterion overestimate the fracture strains while the FLCs predicted by the Oh criterion and the Brozzo criterion match to the experimental results with higher accuracy. For FLCs on the right hand side, the four ductile fracture criteria fail to assess the fracture strains in biaxial tension conditions. The FLCs predicted with the Oh criterion are in better agreement with the experimental results among the four ductile fracture criteria.

Table 2 The temperature-dependent critical values of the four ductile fracture criteria

Deformation temperature (°C)	Critical values			
	C_1	C_2	C_3	C_4
800	0.70	0.77	0.34	1.38
700	0.53	0.59	0.26	1.10
600	0.48	0.53	0.23	0.92

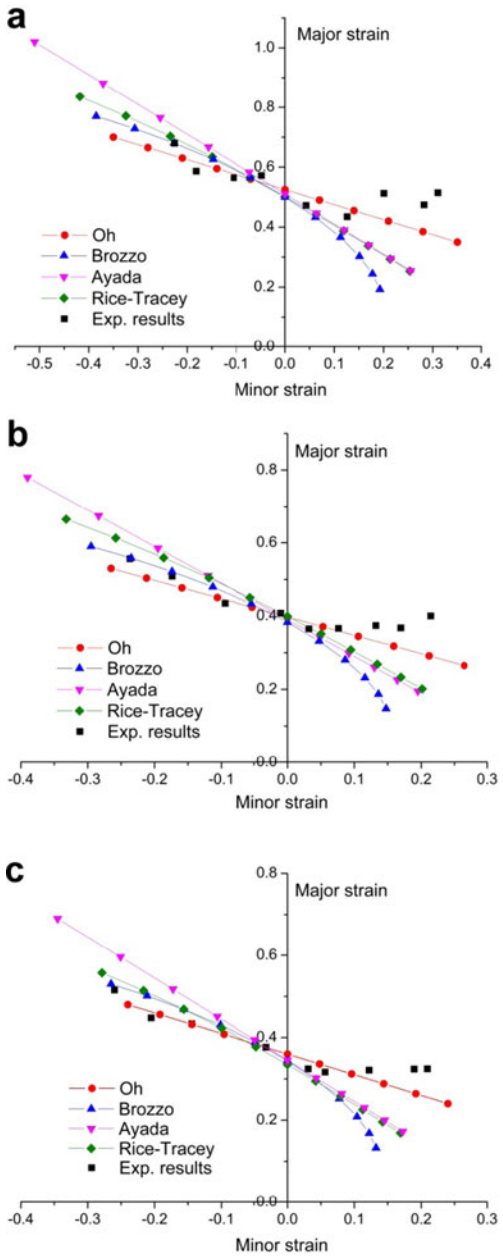

Fig. 5 Comparison of measured FLCs with those predicted by ductile fracture criteria: **a** 800 °C; **b** 700 °C; and **c** 600 °C

3.4.2 Determination of damage parameters

The Lemaitre damage model has been implemented in an explicit thermo-mechanical finite element code to predict ductile damage growth and ductile fracture during deformation process at elevated temperatures. A numerical model of the hot tensile test replicating the thermal and mechanical conditions of the test itself was developed in this code. We assume that the material is deemed as failure when the damage value reaches a critical value D_{cr}, taken to be 0.5. That is, material fails when the variable D/D_{cr} is equal to "1." The three damage parameters at fixed values of temperature and strain rate

Table 3 The temperature and strain rate dependent damage parameters

Strain rate (s^{-1})	Deformation temperature (°C)	p_D	s	S
0.01	800	5.98×10^{-3}	1.976	0.150
	750	7.04×10^{-3}	1.846	0.171
	700	7.32×10^{-3}	1.642	0.322
	650	6.83×10^{-3}	1.802	0.285
0.1	800	8.19×10^{-3}	1.714	0.269
	750	9.43×10^{-3}	1.520	0.364
	700	1.19×10^{-2}	1.359	0.702
	650	8.71×10^{-3}	1.578	0.616
1	800	8.95×10^{-3}	0.904	1.259
	750	1.17×10^{-2}	0.724	1.501
	700	1.39×10^{-2}	0.577	1.745
	650	1.03×10^{-2}	0.783	1.403

were identified by minimizing the difference between the numerical force–displacement curve and the experimental one based on an optimization analysis. And, the commercial optimization software ISIGHT was employed for the optimization analysis. The optimization method used in this research was "Pointer," which is a hybrid combination of four optimization methods: an evolutionary algorithm, the Nelder and Mead downhill simplex method, sequential quadratic programming, and a linear solver.

The determined values of the damage parameters are listed in Table 3. And, a comparison of calculated with experimental curves is shown in Fig. 6. Good agreement is achieved for all the temperatures and strain rates. It can be observed that the flow stress increases significantly with decreasing temperature and increasing strain rate, which is similar to what is commonly observed of other sheet metals. And, at the end of deformation, the flow stress decreases due to damage softening which dominates until the final failure is achieved.

As an example, Fig. 7 shows the distribution of damage for different displacements for the specimen deformed at 800 °C for a strain rate of 0.1 s^{-1}. The figure illustrates that the CDM-based Lemaitre model can well predict necking phenomenon. And, a macroscopic crack is generated and the sample

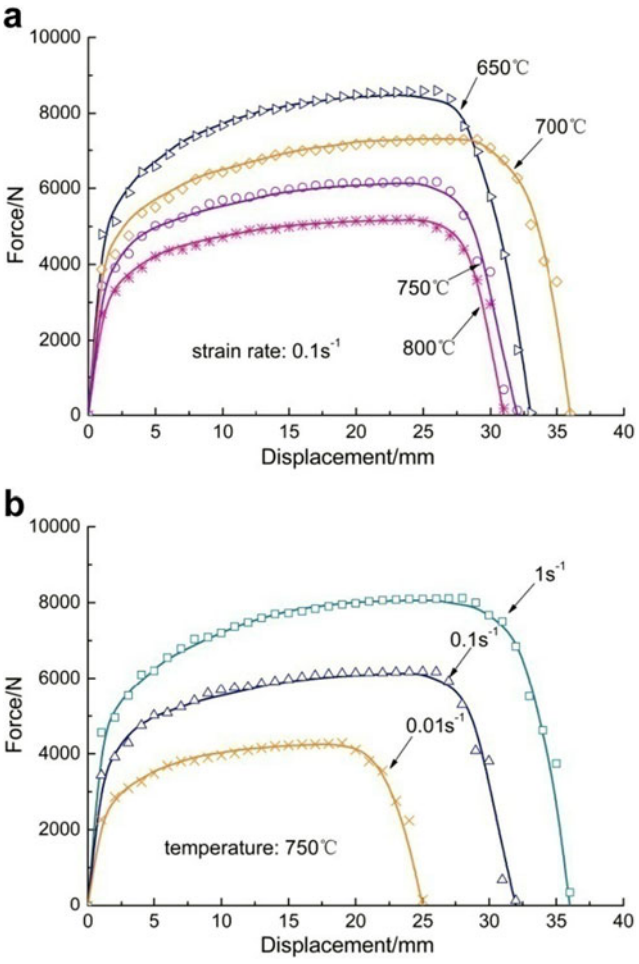

Fig. 6 Comparison of numerical (*symbols*) and experimental (*solid curves*) force–displacement curves for 22MnB5 steel at **a** different temperatures and **b** different strain rates

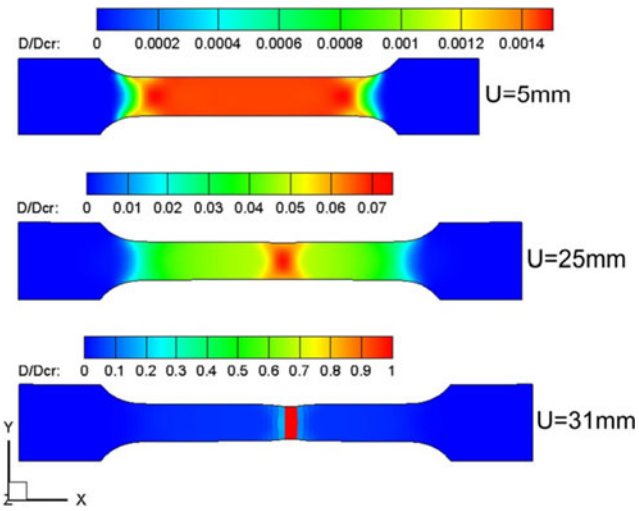

Fig. 7 Damage distribution of the specimen deformed at 800 °C for a strain rate of 0.1 s^{-1}

becomes invalid at a displacement of 31.0 mm. It can be seen that the rupture facies is perpendicular to the tensile direction, which is in good agreement with the experimental result in Fig. 4b.

4 Numerical simulation and verification experiment

The objective of the numerical simulation was a comparative study of the failure prediction of 22MnB5 steel during hot stamping. In general, the initiation and growth of crack occur in the forming stage because of the inapposite process conditions. So the heating and quenching stages were ignored in this study. In addition, in order to guarantee the ultra-high strength of the final part, the blank should maintain a fully metastable austenite state during the deformation operation. Therefore, the phase transitions in the forming stage were also neglected. In this study, the four ductile fracture criteria and the CDM-based Lemaitre damage model with their material parameters determined through the above described procedures were respectively implemented to an explicit thermo-mechanical finite element code and utilized to predict the ductile fracture of a sheet metal part manufactured by the hot stamping process. The finite element code is based on the von Mises isotropic yield function to model plastic deformation with isotropic hardening. The numerical analysis considered an automotive B-pillar hot stamped. The finite element model is shown in Fig. 8 and it is made up of four components: the die, blank, blank holder, and punch. In the model, the blank sheet was meshed using Belytschko–Tsay shell elements [35], while the tools were modeled as rigid elements.

Although the various ductile fracture criteria are valid only under the fixed condition of temperature, we assume that they can be generalized for non-isothermal deformation. Therefore, in order to apply the ductile fracture criterion to numerical analysis of the non-isothermal hot stamping process, a normalized integral value is defined as the following summation [36]:

$$C_{nc} = \sum_{k=1}^{M} \frac{F(\sigma_{ij})_k \Delta\bar{\varepsilon}_k^p}{C(T_k)} = 1 \tag{14}$$

where C_{nc} denotes the normalized integral value, k is the deformation step, M is the total number of the time steps, and T_k is the temperature at the kth deformation step. The value of C_{nc} is calculated at integration points as deformation goes on. The critical failure criterion defined in Eq. (14) attests that the material is deemed to fracture when this value reaches to the unity.

For the numerical prediction using the Lemaitre damage model, an accumulative principle was adopted to determine when damage initiates during non-isothermal hot stamping condition with variable strain rates. Assuming finite time increments, damage starts when the following condition is satisfied

$$\sum_{k=1}^{M} \frac{\Delta\bar{\varepsilon}_k^p}{p_D^k(\dot{\varepsilon}, T)} = 1 \tag{15}$$

where $\Delta\bar{\varepsilon}_k^p$ and $p_D^k(\dot{\varepsilon}, T)$ are the equivalent plastic strain increment and the temperature- and strain-rate-dependent damage threshold at the kth step, respectively.

The modified Norton–Hoff equation was used to describe the rheological behavior of 22MnB5 steel at elevated temperatures. The mechanical properties of the blank, including Young's modulus and Poisson's ratio, were defined to be temperature dependent and were given by Shapiro [37]. And, the thermal properties of the blank, including thermal conductivity and specific heat, were also defined to include temperature dependency and were taken from data published by Holman [38]. The thermal expansion coefficient was taken to be $1.3\times10^{-5}K^{-1}$. The Coulomb's law was used to describe the friction between the blank sheet and the tools, and the friction coefficient used for the forming simulation was set to 0.4, as per recommendation from George et al. [39]. The heat transfer coefficient between the blank and tools was obtained from Kim et al. [40] for similar condition. The air cooling of the blank was modeled with a convection and radiation boundary condition to an ambient surrounding of 25 °C. An effective heat transfer coefficient was defined to combine both convection and radiation effects, as reported in Shapiro [37]. The initial temperature of the blank was 800 °C and the tools were kept at 50 °C. And, the forming time was 1.6 s.

Figure 9a shows the hot stamping tools with cooling system. The proper blank holding force for excellent formability of the B-pillar is 30 kN, and the formed part is shown in Fig. 9b. And, Fig. 10 presents the temperature distribution of

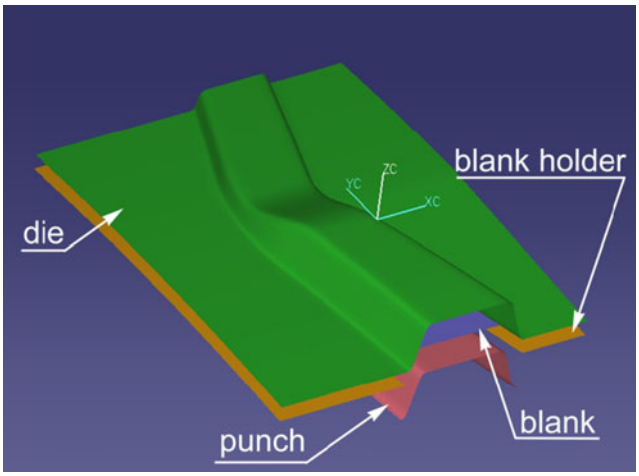

Fig. 8 The finite element model of the hot stamping of B-pillar

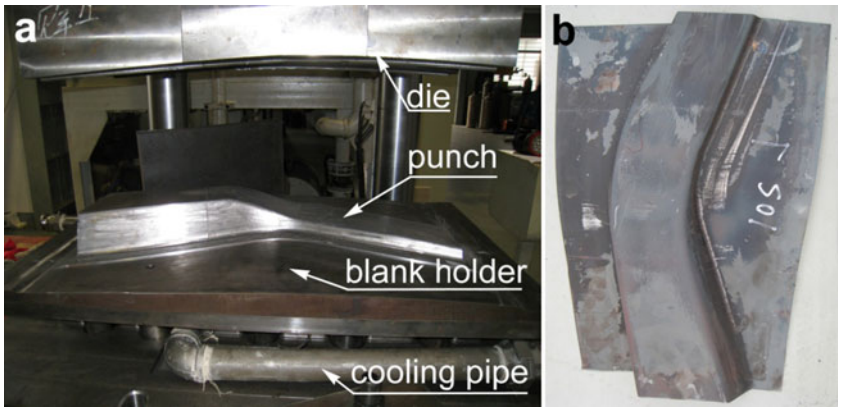

Fig. 9 **a** The hot stamping tools; **b** the formed B-pillar with excellent formability

the B-pillar after the stamping stage. In this study, the blank holding force of 100 kN has been deliberately selected so that damage propagation and fracture initiation can be easily observed.

5 Results and discussion

5.1 The fracture location

To judge whether a fracture criterion is suitable for predicting the occurrence of crack in a metal forming process, the fracture contour of the workpiece in the numerical simulations should be in accordance with that of the experiment well. Figure 11a–d shows the distributions of the normalized integral values of the B-pillar after hot stamping stage with the four uncoupled phenomenological models: Oh, Brozzo, Ayada, and Rice–Tracey. In these figures, the maximum normalized integral values for these models all reach the unity which represents material failure. It can be observed that in the simulations when the stamping process is finished, the locations of the maximum integral values are all near the rounded corner close to the top of formed B-pillar except the Brozzo criterion. For the Brozzo criterion, the maximum normalized integral value locates at the lower part of the left side wall. For the Oh criterion, the Ayada criterion, and the Rice–Tracey criterion, the cracks initiate in the middle part of the B-pillar and then propagate from the middle part to the rear part. And, the calculated result using the Ayada criterion is very similar to that predicted by the Rice–Tracey criterion. These three criteria differ in the fracture degree reflected in the length of crack.

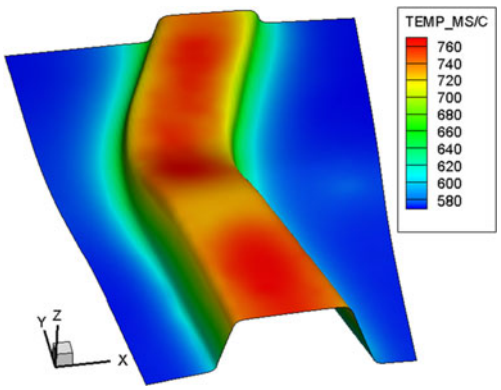

Fig. 10 The temperature distribution of the B-pillar after the stamping stage

Figure 12 shows the damage distribution of the B-pillar by using CDM-based Lemaitre model after stamping which obviously shows that fractures occur near the rounded corner close to the top of formed part. And, it is similar to the calculated result using the Oh criterion.

Figure 13 presents the experimentally observed fracture located at the B-pillar after the hot stamping process under 100-kN blank holding force. In the experiment, crack appears around the punch rounded corner, and the deformation is localized there. The fracture locations predicted by the Oh criterion and CDM-based Lemaitre model are close to the experimental result. The crack lengths predicted by the Ayada criterion and the Rice–Tracey criterion are much longer than the experimental value. However, the Brozzo criterion fails to predict the fracture position.

5.2 The moment of crack initiation

Figure 14 shows the evolution of maximum normalized integral values of the material point located at the rupture region for the three effective ductile fracture criteria: Oh, Ayada, and Rice–Tracey. As can be seen in this figure, the normalized integral values initiate almost at the same time (the die displacement is equal to 17.44 mm) for different criteria. With further increase in the die displacement, they all increase. The normalized integral values for the Ayada criterion and the Rice–Tracey criterion increase much faster than that for the Oh criterion. It is clear that crack occurs when the normalized integral value reaches the unity. The Oh criterion indicates that fracture occurs when the die displacement is 66.69 mm. And,

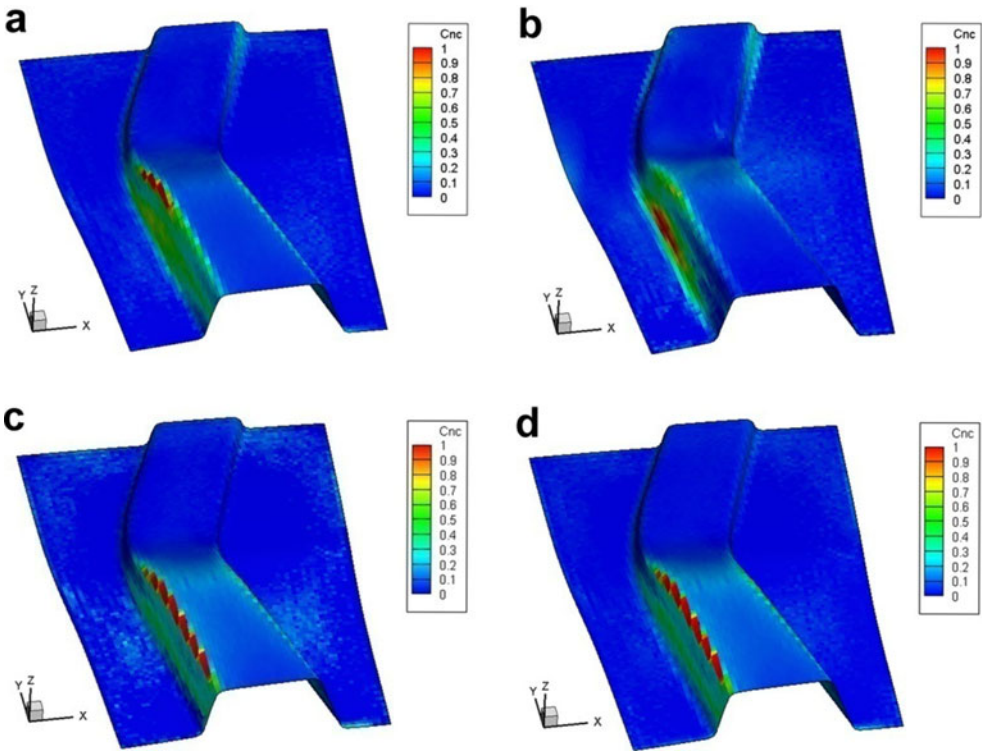

Fig. 11 Distribution of the normalized integral values in numerical simulations using the four ductile fracture criteria: **a** Oh criterion; **b** Brozzo criterion; **c** Ayada criterion; **d** Rice–Tracey criterion

for these three ductile fracture criteria, fracture takes place before the die completes its total stroke.

Figure 15 shows the evolution of maximum damage value of the material point located at the rupture region. The damage initiates at the die displacement of 31.65 mm. And then, the total damage is accumulated non-linearly step by step. The fracture is predicted with CDM-based Lemaitre model when the damage variable reaches the unity. And, the corresponding die displacement is 82.16 mm.

In order to ascertain the moment of crack initiation, the drop of punch force in metal forming process can be thought as an indicator of the crack event undergone in the part [27, 28]. For the uncoupled ductile fracture criterion, the interaction between the strain or stress behavior and the damage is neglected, so the variation of punch force calculated by uncoupled criterion cannot really reflect material failure. Figure 16 shows the comparison between the measured and calculated results by CDM-based Lemaitre model with regard to the punch force versus the die displacement under 100-kN blank holding force. An acceptable agreement between simulation and experiment was found as well. The distance between die and punch is in close proximity after the die displacement of 85 mm, and the punch force increases sharply due to the impact between them. Therefore, in order to present the effect of material damage well, the segment beyond the die displacement of 85 mm was cut out. The die displacement is 80.55 mm when fracture occurs, which is close to the result obtained from Fig. 15. Therefore, it can be concluded that the CDM-based Lemaitre model, rather than the ductile fracture criteria, can predict accurately the moment of crack initiation.

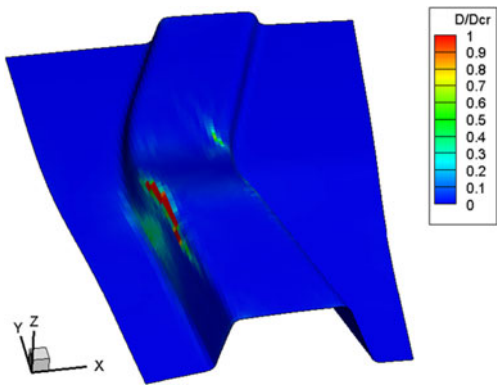

Fig. 12 Damage distribution in numerical simulation using CDM-based Lemaitre model

Fig. 13 The experimental final fracture located at the B-pillar

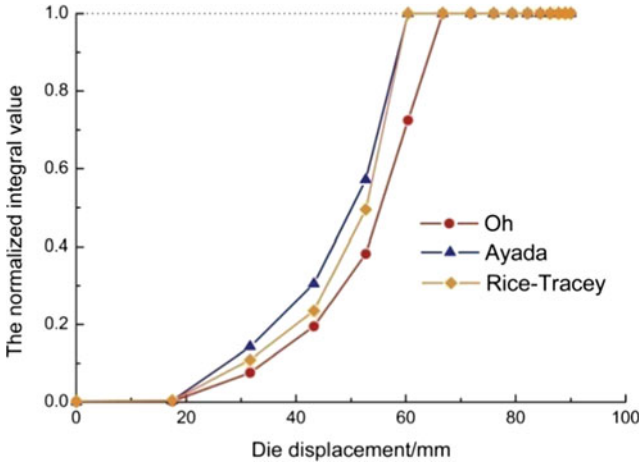

Fig. 14 The evolution of maximum normalized integral values of the material point located at the rupture region for the three ductile fracture criteria

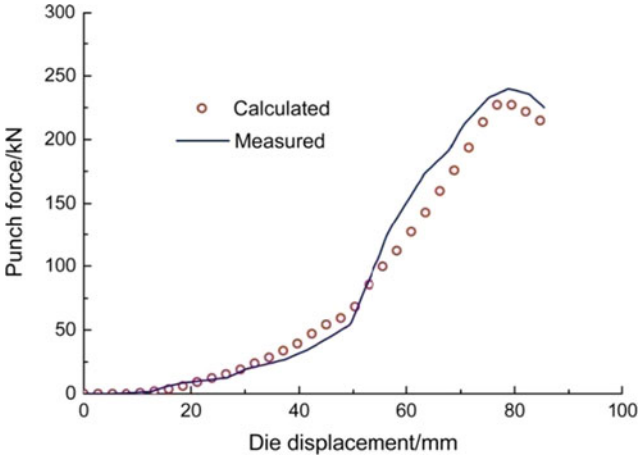

Fig. 16 Comparison between measured and calculated results of punch force–die displacement using CDM-based Lemaitre model

6 Conclusion

This study is devoted to a finite element prediction of ductile damage and fracture within the workpiece during hot stamping processes. The prediction capacity of ductile fracture criteria and CDM-based Lemaitre model for ductile fracture was compared. The FLCs predicted by the four ductile fracture criteria were compared to experimental results to determine the average temperature-dependent critical values. The mechanical properties of 22MnB5 steel at elevated temperatures and damage parameters sensitive to temperature and strain rate were identified by using uniaxial hot tensile tests. These calibrated models were employed into an explicit thermo-mechanical finite element code for hot stamping analysis of an automotive B-pillar part. The fracture location and fracture moment of the hot-stamped B-pillar part were predicted. Comparison between the numerical and experimental results shows that both the Oh criterion and the CDM-based Lemaitre model predict the fracture location reasonably well. However, the Brozzo criterion failed to predict the fracture position. The Ayada criterion and Rice–Tracey overpredicted the fracture degree. The fracture moment predicted with the CDM-based Lemaitre model was in better agreement with experiment than that predicted with the four ductile fracture criteria. Hence, finite element analysis in conjunction with CDM-based Lemaitre model can be well applied as a reliable tool to predict ductile fracture in hot stamping processes.

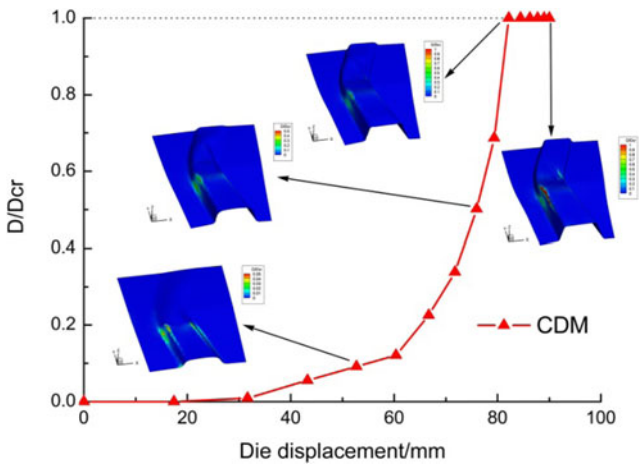

Fig. 15 The evolution of maximum damage value of the material point located at the rupture region

Acknowledgments The authors would like to thank the reviewers for their constructive comments. This research is financially supported by the National Natural Science Foundation of China (No. 11272075), China's Post-doctoral Science Fund (2014 M561223), and Basic Scientific Research Fund of the Central University (DUT14ZD224, DUT14RC(3)032).

References

1. Liu HS, Lei CX, Xing ZW (2013) Cooling system of hot stamping of quenchable steel BR1500HS: optimization and manufacturing methods. Int J Adv Manuf Technol 69:211–223
2. Kim HY, Park JK, Lee MG (2014) Phase transformation-based finite element modeling to predict strength and deformation of press-hardened tubular automotive part. Int J Adv Manuf Technol 70:1787–1801
3. Marciniak Z, Kuczyński K (1967) Limit strains in the processes of stretch-forming sheet metal. Int J Mech Sci 9:609–620
4. Nakazima K, Kikuma T, Hasuka K (1968) Study on the formability of steel sheets. Yawata Tech Rep 264:8517–8530
5. Bariani PF, Bruschi S, Ghiotti A, Turetta A (2008) Testing formability in the hot stamping of HSS. Annals CIRP 57:265–268
6. Pellegrini D, Lechler J, Ghiotti A, Bruschi S, Merklein M (2009) Interlaboratory comparison of forming limit curves for hot stamping of high strength steels. Key Eng Mater 410:297–304
7. Min JY, Lin JP, Li JY, Bao WH (2010) Investigation on hot forming limits of high strength steel 22MnB5. Comput Mater Sci 49:326–332

8. Li HZ, Wu X, Li GY (2013) Prediction of forming limit diagrams for 22MnB5 in hot stamping process. J Mater Eng Perform 22: 2131–2140
9. Li FF, Fu MW, Lin JP, Wang XN (2014) Experimental and theoretical study on the hot forming limit of 22MnB5 steel. Int J Adv Manuf Technol 71:297–306
10. Güler H, Ertan R, Özcan R (2014) Investigation of the hot ductility of a high-strength boron steel. Mater Sci Eng A 608:90–94
11. Cockcroft MG, Latham DJ (1968) Ductility and the workability of metals. J Inst Met 96:33–39
12. Oh SI, Chen CC, Kobayashi S (1979) Ductile fracture in axisymmetric extrusion and drawing-part 2: workability in extrusion and drawing. J Manuf Sci Eng 101:36–44
13. Brozzo P, Deluca B, Rendina R (1972) A new method for the prediction of formability in metal sheets. In: Proceedings of the International deep drawing research group on sheet metal forming and formability, October, Amsterdam
14. Ayada M, Higashino T, Mori K (1987) Central bursting in extrusion of inhomogeneous materials. Adv Technol Plasticity 1:553–558
15. Rice JR, Tracey DM (1969) On the ductile enlargement of voids in triaxial stress fields. J Mech Phys Solids 17:201–217
16. Clift SE, Hartley P, Sturgess C, Rowe GW (1990) Fracture prediction in plastic deformation processes. Int J Mech Sci 32:1–17
17. Ozturk F, Lee D (2004) Analysis of forming limits using ductile fracture criteria. J Mater Process Technol 147:397–404
18. Takuda H, Mori K, Fujimoto H, Hatta N (1996) Prediction of forming limit in deep drawing of Fe/Al laminated composite sheets using ductile fracture criterion. J Mater Process Technol 60:291–296
19. Takuda H, Mori K, Takakura N, Yamaguchi K (2000) Finite element analysis of limit strains in biaxial stretching of sheet metals allowing for ductile fracture. Int J Mech Sci 42:785–798
20. Liu HS, Yang YY, Yu ZQ, Sun ZZ, Wang YZ (2009) The application of a ductile fracture criterion to the prediction of the forming limit of sheet metals. J Mater Process Technol 209:5443–5447
21. Lou YS, Huh H, Lim SJ, Pack KH (2012) New ductile fracture criterion for prediction of fracture forming limit diagrams of sheet metals. Int J Solids Struct 49:3605–3615
22. Ogawa N, Shiomi M, Osakada K (2002) Forming limit of magnesium alloy at elevated temperatures for precision forging. Int J Mach Tools Manuf 42:607–614
23. Gurson AL (1977) Continuum theory of ductile rupture by void nucleation and growth: part I-yield criteria and flow rules for porous ductile media. J Eng Mater Technol 99:2–15
24. Tvergaard V, Needleman A (1984) Analysis of the cup-cone fracture in a round tensile bar. Acta Metall 32:157–169
25. Lemaitre J (1985) A continuous damage mechanics model for ductile fracture. J Eng Mater Technol 107:83–89
26. Abbassi F, Belhadj T, Mistou S, Zghal A (2013) Parameter identification of a mechanical ductile damage using Artificial Neural Networks in sheet metal forming. Mater Des 45:605–615
27. Khelifa M, Oudjene M, Khennane A (2007) Fracture in sheet metal forming: effect of ductile damage evolution. Comput Struct 85: 205–212
28. Aboutalebi FH, Farzin M, Poursina M (2011) Numerical simulation and experimental validation of a ductile damage model for DIN 1623 St14 steel. Int J Adv Manuf Technol 53:157–165
29. Mkaddem A, Hambli R, Potiron A (2004) Comparison between Gurson and Lemaitre damage models in wiping die bending processes. Int J Adv Manuf Technol 23:451–461
30. Bariani PF, Bruschi S, Ghiotti A (2012) Advances in predicting damage evolution and fracture occurrence in metal forming operations. J Manuf Process 14:495–500
31. Mohamed MS, Foster AD, Lin JG, Balint DS, Dean TA (2012) Investigation of deformation and failure features in hot stamping of AA6082: experimentation and modelling. Int J Mach Tools Manuf 53:27–38
32. Takuda H, Mori K, Hatta N (1999) The application of some criteria for ductile fracture to the prediction of the forming limit of sheet metals. J Mater Process Technol 95:116–121
33. Lemaitre J, Desmorat R (2005) Engineering damage mechanics: ductile, creep, fatigue and brittle failures. Springer, Cachan
34. Hochholdinger B, Grass H, Lipp A, Hora P (2009) Modeling and determination of flow curves for the simulation of hot forming. In: Proceedings of the International Deep Drawing Research Group on Sheet Metal Forming and Formability, June, Colorado, pp. 659–669
35. Belytschko T, Tsay CS (1983) A stabilization procedure for the quadrilateral plate element with one-point quadrature. Int J Numer Methods Eng 19:405–419
36. Kim WJ, Kim HK, Kim WY, Han SW (1983) Temperature and strain rate effect incorporated failure criteria for sheet forming of magnesium alloys. Mater Sci Eng A 488:468–474
37. Shapiro AB (2009) Using LS-Dyna for hot stamping. 7th European LS-Dyna Conference, May, Salzburg
38. Holman JP (2010) Heat transfer. McGraw-Hill, New York
39. George R, Bardelcik A, Worswick MJ (2012) Hot forming of boron steels using heated and cooled tooling for tailored properties. J Mater Process Technol 212:2386–2399
40. Kim HG, Son HS, Kang SY, Park SH (2006) Thermal-mechanical coupled simulation on the forming of hot press formed part. In: Proceedings of the International deep drawing research group on sheet metal forming and formability, June, Porto, pp. 349–354